

# PROPERTIES OF THE SCUBA-2 850 $\mu\text{m}$ SOURCES IN THE XMM-LSS FIELD

HYUNJONG SEO<sup>1</sup>, WOONG-SEOB JEONG<sup>1,2</sup>, SEONG JIN KIM<sup>1</sup>, JEONGHYUN PYO<sup>1</sup>, MIN GYU KIM<sup>3</sup>, JONGWAN KO<sup>1,2</sup>, MINJIN KIM<sup>1,2</sup>, AND SAM KIM<sup>4</sup>

<sup>1</sup>Korea Astronomy and Space Science Institute, 776 Daedukdae-ro, Yuseong-gu, Daejeon 34055, Korea; [hjseo@kasi.re.kr](mailto:hjseo@kasi.re.kr)

<sup>2</sup>Korea University of Science and Technology, 217 Gajeong-ro, Yuseong-gu, Daejeon 34113, Korea

<sup>3</sup>Department of Physics and Astronomy, Seoul National University, 1 Gwanak-ro, Gwanak-gu, Seoul 08826, Korea

<sup>4</sup>Pontificia Universidad Católica de Chile, Casilla 306, Santiago 22, Chile

Received November 14, 2016; accepted December 29, 2016

**Abstract:** We carry out the study of 850  $\mu\text{m}$  sources in a part of the XMM-LSS field. The 850  $\mu\text{m}$  imaging data were obtained by the SCUBA-2 on the James Clerk Maxwell Telescope (JCMT) for three days in July 2015 with an integration time of 6.1 hours, covering a circular area with a radius of 15'. We choose the central area up to a radius of 9'.15 for the study, where the noise distribution is relatively uniform. The root mean square (rms) noise at the center is 2.7 mJy. We identify 17 sources with  $S/N > 3.5$ . Differential number count is estimated in flux range between 3.5 and 9.0 mJy after applying various corrections derived by imaging simulations, which is consistent with previous studies. For detailed study on the individual sources, we select three sources with more reliable measurements ( $S/N > 4.5$ ), and construct their spectral energy distributions (SEDs) from optical to far-infrared band. Redshift distribution of the sources ranges from 0.36 to 3.28, and their physical parameters are extracted using MAGPHYS model, which yield infrared luminosity  $L_{IR} = 10^{11.3} - 10^{13.4} L_{\odot}$ , star formation rate  $\text{SFR} = 10^{1.3} - 10^{3.2} M_{\odot}\text{yr}^{-1}$  and dust temperature  $T_D = 30 - 53$  K. We investigate the correlation between  $L_{IR}$  and  $T_D$ , which appears to be consistent with previous studies.

**Key words:** galaxies: evolution — submillimeter: galaxies

## 1. INTRODUCTION

Along with UV and optical light, re-emitted thermal emission of starlight by dust is a significant tracer of star formation in the Universe. Therefore, observations in far-infrared and sub-millimeter wavelength bands are important tools in investigating the evolution of the Universe. Since the study of Smail et al. (1997) for sub-millimeter galaxies (SMGs) at high redshift, observations of SMGs using space and ground-based telescopes have been conducted for the study of the formation and evolution of galaxies.

Median redshifts of 850 & 870  $\mu\text{m}$  sources in most studies are around  $\langle z \rangle = 2$  or larger (Chapman et al. 2005; Wardlow et al. 2011; Casey et al. 2013). Number count at sub-millimeter wavelength bands (Blain et al. 1999; Beelen et al. 2008; Knudsen et al. 2008; Casey et al. 2013; Chen et al. 2013a; Karim et al. 2013) has been used to provide constraints on theoretical studies of galaxy evolution (Lagache et al. 2003; Swinbank et al. 2008; Hayward et al. 2013) and whether extragalactic background light (EBL) can be attributed to the contribution of undetected faint galaxies (Knudsen et al. 2008; Zemcov et al. 2010; Chen et al. 2013b). Studies of the properties of SMGs show extreme physical parameters like those of ultraluminous infrared galaxies (ULIRGs) in the local Universe, e.g., infrared luminosity  $L_{IR} > 10^{12} L_{\odot}$ ,  $\text{SFR} = 100 - 1000 M_{\odot}\text{yr}^{-1}$  (Coppin et al. 2008; Chapman et al. 2010; da Cunha et al. 2015).

Relationships between physical parameters, e.g.,  $L_{IR}$  – dust temperature  $T_D$  relation and its evolution (Chapman et al. 2005; Hwang et al. 2010b; Magnelli et al. 2012; Symeonidis et al. 2013; Smolčić et al. 2015), have been also investigated.

ULIRGs in the local Universe are generally known to be formed by merger processes (Sanders et al. 1988), while the major star formation process of SMGs at high redshift is still uncertain. Several studies show that SMGs are correlated with merger events by considering their morphologies and kinematics (Engel et al. 2010; Alaghband-Zadeh et al. 2012). On the other hand, Targett et al. (2013) found that some SMGs are normal star forming galaxies with disk-like morphology using near-infrared imaging data. Hayward et al. (2013) reproduced observed number count at sub-millimeter band using three kinds of populations such as isolated disk galaxies, galaxy-pairs and merger-induced starbursts. These studies illustrate that it is hard to explain the nature of SMGs at high redshift by introducing a single population such as merger-induced starbursts. More observational studies are necessary to understand physical properties of SMGs and their contributions to the evolution of the Universe.

Protoclusters, galaxy overdense region at high redshift ( $z > 2$ ), are thought to be linked with the present day galaxy clusters (Venemans et al. 2002; Ouchi et al. 2004; Overzier et al. 2006). Compared to blank-fields, protoclusters are efficient sites for the observational study of SMGs because there are plenty number

of SMGs in a confined area and high number density of SMGs leads to frequent interactions with each other. Thus these form good laboratories for the study of various types of SMGs and their evolution (Venemans et al. 2007). The objective of this study is a pilot research for identifying a candidate protocluster in the XMM-LSS field. We focus on a triple SMG system which is a red object selected by HerMES/SPIRE (55, 88 and 94 mJy at 250, 350 and 500  $\mu\text{m}$ , respectively) and finally resolved into three components by APEX/LABOCA<sup>1</sup> observation (Kim et al., in preparation). Redshifts of two of them were measured spectroscopically as  $z = 4.44$ . The third component and neighboring objects around the triple system were also identified as high redshift objects by their colors in far-infrared and sub-millimeter bands. Therefore, this triple SMG system may be a protocluster at  $z = 4.44$ . If so, physical properties of SMGs in this region will be different compared to SMGs in blank-fields. For example, peak and dispersion of the redshift distribution of SMGs in the protocluster may be different with those in a blank-field, and number count of SMGs in the protocluster may be overdense. In this study, as a pilot study for identifying the candidate protocluster, we investigate number count and physical properties of SMGs in blank-field located 12'7 away from the triple SMG system (refer to Figure 1). Because 12'7 at  $z = 4.44$  corresponds to 5.06 Mpc, the FOV of the imaging data in this study can be treated as blank-field that is rarely or only partially related with the possible protocluster around the triple SMG system by assuming the triple SMG system is a center of the candidate protocluster and a typical size of the protocluster is a diameter of  $\sim 2\text{--}5$  Mpc (Miley et al. 2004; Intema et al. 2006; Venemans et al. 2007). Result of this study can provide useful criteria for identifying the candidate protocluster around the triple SMG system.

In the XMM field, studies for SMGs usually have been conducted using sub-millimeter imaging data in SCUBA Half-Degree Extragalactic Survey (SHADES; Mortier et al. 2005) program which is blank-field extragalactic survey taken by the SCUBA on the JCMT. Subaru/XMM-Newton Deep Field (SXDF) centered at  $(\alpha_{2000}, \delta_{2000}) = (02^h18^m00^s, -05^\circ00'00'')$  is one of two regions in SHADES where number count (Coppin et al. 2006), redshift distribution (Aretxaga et al. 2007; Ivison et al. 2007; Clements et al. 2008) and physical parameters of SMGs (Clements et al. 2008) were investigated. In this study, we also investigate number count and physical properties of SMGs in blank-field using 850  $\mu\text{m}$  imaging data centered at  $(\alpha_{2000}, \delta_{2000}) = (02^h18^m07^s, -04^\circ03'42'')$  in the XMM-LSS field taken by Submillimeter Common User Bolometer Array-2 (SCUBA-2; Holland et al. 2013). Results for the SXDF as well as those for other blank-fields can be compared with the results in this study. Multi-wavelength surveys from UV to radio bands for the field in this study (Table 1) are available, which are useful to estimate SEDs of sub-millimeter sources.

<sup>1</sup><http://www.apex-telescope.org/bolometer/laboca/>

**Table 1**  
Multi-wavelength surveys for the field in this study

Survey	$\lambda$ ( $\mu\text{m}$ )	Resolution (arcsec)	Sensitivity <sup>a</sup> (mJy)
<i>XMM-Newton</i> <sup>b</sup>	0.5-2 keV	6	$3 \times 10^{-15}$
	2-12 keV	6	$1 \times 10^{-14}$
<i>GALEX</i> <sup>c</sup>	0.153	4.5	$3.6 \times 10^{-4}$
	0.227	6.0	$3.6 \times 10^{-4}$
CFHT <sup>d</sup>	0.375	0.831	$6.0 \times 10^{-4}$
	0.487	0.832	$5.2 \times 10^{-4}$
	0.630	0.862	$9.8 \times 10^{-4}$
	0.770	0.742	$12 \times 10^{-4}$
	0.890	0.818	$27 \times 10^{-4}$
VISTA <sup>e</sup>	0.878	0.9	0.002
	1.021	0.9	0.004
	1.254	0.9	0.005
	1.646	0.9	0.009
	2.149	0.9	0.012
UKIDSS <sup>f</sup>	1.248	<1.3	0.002
	2.201	<1.3	0.003
<i>WISE</i> <sup>g</sup>	3.4	6.1	0.08
	4.6	6.4	0.11
	12	6.5	1
	22	12	6
<i>Spitzer</i> /IRAC <sup>h</sup>	3.6	2.1	0.004
	4.5	2.1	0.005
	5.8	2.1	0.048
	8.0	2.5	0.038
/MIPS <sup>h</sup>	24	6	0.230
HerMES/PACS <sup>i</sup>	100	6.8	49.9
	160	11.4	95.1
/SPIRE <sup>i</sup>	250	18.2	25.8
	350	24.9	21.2
	500	36.3	30.8
NVSS <sup>j</sup>	21cm	45	0.45

<sup>a</sup> It represents  $5\sigma$  sensitivity except *XMM-Newton*, CFHT and NVSS.

<sup>b</sup> Melnyk et al. (2013). Sensitivity represents 50% detection probability with the unit of  $\text{erg cm}^{-2} \text{s}^{-1}$ .

<sup>c</sup> Martin et al. (2005)

<sup>d</sup> [http://terapix.iap.fr/cpl/t0007/table\\_syn\\_T0007.html](http://terapix.iap.fr/cpl/t0007/table_syn_T0007.html). Sensitivity is 80% completeness limit for extended object.

<sup>e</sup> Edge et al. (2013) and Sutherland et al. (2015)

<sup>f</sup> Lawrence et al. (2007)

<sup>g</sup> Wright et al. (2010)

<sup>h</sup> Lonsdale et al. (2003) and <http://swire.ipac.caltech.edu/swire/astronomers/program.html>

<sup>i</sup> Oliver et al. (2012)

<sup>j</sup> Condon et al. (1998). It represents  $1\sigma$  sensitivity.

Due to large beam size of the SCUBA-2 (FWHM at 850  $\mu\text{m}$   $\sim 14''$ ), investigation of SMG is challenging work. Observation data with low angular resolution due to large beam size is less effective for the study of number count because of blending problem with neighbors and large number of undetected faint sources in a single beam. In addition, large positional uncertainty of the source due to large beam size also causes problems in

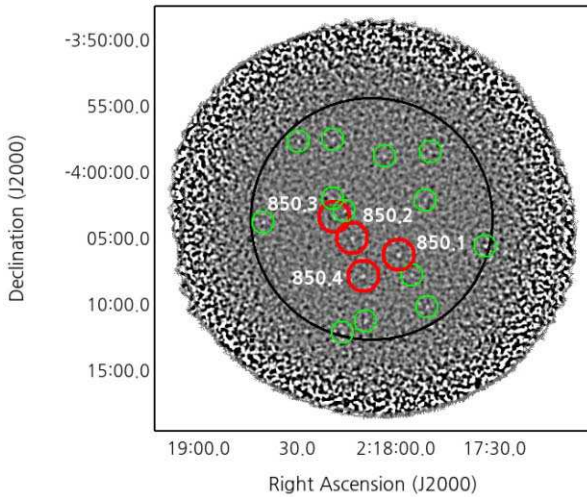


**Figure 1.** Mosaic image of the SCUBA-2 850  $\mu\text{m}$ . Green circles and red circles show the 17 sources detected with  $S/N > 3.5$ , which were used for the number count study. Red circles with IDs are sources with  $S/N > 4.5$ , which were selected for the study of individual sources. In this study, we limited our analysis to the area up to the radius of  $9'15''$  (black large circle) where rms noise becomes 1.5 times the value at the center.

the identification of counterparts in multi-wavelength bands. In order to overcome these difficulties, we conducted simulations carefully to correct the contribution of undetected sources and random noise. Moreover, identification of counterparts in multi-wavelength bands was performed using likelihood ratio analysis which considers magnitudes as well as positions of counterparts. The identified counterpart was further investigated to confirm its validity using available information for the counterpart.

This paper is organized as follows. In §2, we present observation data of the XMM-LSS field and pre-processing of raw data. In §3, simulations for the correction of the raw data are presented, and differential number count of 850  $\mu\text{m}$  sources is described. Matching multi-wavelength catalogs and building SEDs of galaxies are treated in §4. Results of this study are discussed in the final section. In this study, we assume a flat Universe with a set of cosmological parameters:  $H_0 = 70 \text{ km s}^{-1} \text{ Mpc}^{-1}$ ,  $\Omega_M = 0.3$  and  $\Omega_\Lambda = 0.7$ .

## 2. OBSERVATION AND DATA REDUCTION

We obtained the observation data in a part of the XMM-LSS field taken by the SCUBA-2 instrument on the JCMT at 850  $\mu\text{m}$  wavelength band (Program ID: M15AI137). PONG-900 was used in observing mode, which is one of the scan patterns of the SCUBA-2 and effective for mapping larger area than field of view (FOV) of the instrument (Holland et al. 2013). In a single mapping procedure, PONG-900 covers an area of  $900'' \times 900''$  with a scan velocity of  $280''/\text{sec}$ . Observations were carried out for three nights in July 2015 with total integration time of 6.1 hours. The total FOV covered by the observation is a circular area of  $15'$  radius

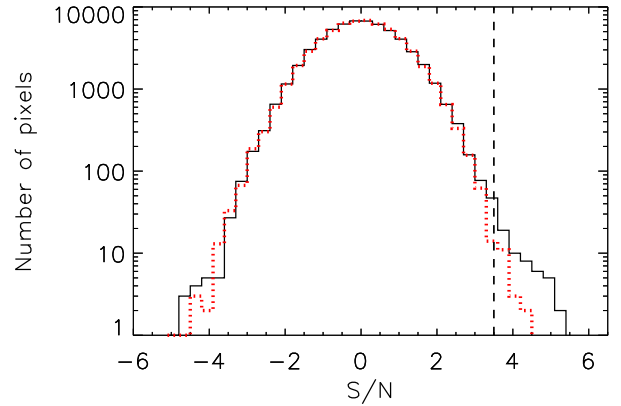


**Figure 2.** Histograms of S/N map for the mosaic image (black solid line) and noise map (red dotted line). An excess of the solid line above the dotted line at the right side represents the contribution of sources in the mosaic image. The noise map was made using subset analysis. Vertical dashed line represents the detection threshold of  $S/N = 3.5$ .

centered at  $(\alpha_{2000}, \delta_{2000}) = (02^h 18^m 07^s, -04^\circ 03' 42'')$ , and the pixel scale of the image is  $4''$  (Table 2).

Pre-processing of the observation data was conducted using various packages in STARLINK<sup>2</sup> software, an automated data reduction pipeline. First of all, observation data were reduced and stacked for each date separately using MAKEMAP recipe in the SMURF package (Chapin et al. 2013) with *dimconfig\_blank\_field.lis* which is a configuration file for blank-field survey and has options suitable for the detection of faint sources. Because the flux conversion factor (FCF) which translates pW to  $\text{Jy beam}^{-1}$  varies on time, data stacking was carried out for each date separately and different FCF was applied to the data for each date. FCF for each date was estimated using calibration data<sup>3</sup> taken on the same date. Among various calibration objects for the SCUBA-2 (Dempsey et al. 2013), we used a calibrator which is the nearest one to the science observation in time for each date. We selected CRL 2688, CRL 618 and Uranus as calibrators for the date of 2nd, 15th and 16th July 2015, respectively, and estimated FCF for each date, resulting in 636.22, 668.35 and 701.82  $\text{Jy pW}^{-1} \text{ beam}^{-1}$ , respectively. Matched-filter procedure was applied on the image to improve the detectability of point sources using SCUBA2\_MATCHED\_FILTER recipe in PICARD package. This recipe involves two parts. First, a background map is generated by convolving the observation image using Gaussian function with  $\text{FWHM} = 30''$ . Then, the background map is subtracted from the observation image. Secondly, the observation image is convolved with a Gaussian function with  $\text{FWHM} = 14''$  to improve detectability of point sources. The observation images for three days were then coad-

<sup>2</sup>STARLINK is publicly available on the Web at <http://starlink.eao.hawaii.edu/starlink>

<sup>3</sup>Calibration data of the SCUBA-2 are publicly available on the Web at <http://www.eaoobservatory.org/sc2cal>

**Table 2**  
SCUBA-2 850  $\mu\text{m}$  observations in the XMM-LSS field

RA(J2000) DEC(J2000)	02 <sup>h</sup> 18 <sup>m</sup> 07 <sup>s</sup> -04°03′42″		
FOV (arcmin <sup>2</sup> )	263.02 <sup>a</sup>		
Observing mode	PONG-900		
Observation date (year/month/day)	2015/07/02	2015/07/15	2015/07/16
Integration time (hr)	1.5	1.6	3.0
Calibrator	CRL 2688	CRL 618	Uranus
FCF (Jy pW <sup>-1</sup> beam <sup>-1</sup> )	636.22	668.35	701.82

<sup>a</sup> It corresponds to the circular area with the radius of 9′15.

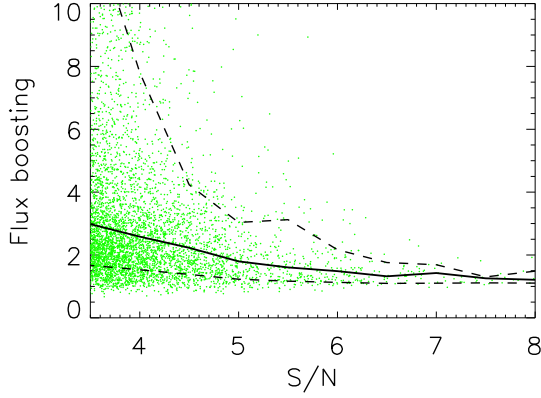


**Figure 3.** Flux boosting as a function of S/N. Small dot represents a ratio of measured flux density to injected flux density of individual artificial object. Solid line and dashed lines represent median and  $\pm 34\%$  confidence interval, respectively. Because rms noise varies with the position in the mosaic image due to the property of the observing mode, we estimated flux boosting as a function of S/N instead of as a function of flux density. Observed raw flux density of 850  $\mu\text{m}$  source in the observation image was deboosted using median (solid line), and an error of the deboosted flux density was estimated using  $\pm 34\%$  confidence interval (dashed lines).

ded to obtain the final mosaic image (Figure 1) using MOSAIC\_JCMT\_IMAGES recipe in PICARD package. For the source detection, a signal-to-noise ratio (S/N) map was generated using MAKESNR recipe in KAPPA package.

To make a noise map, we used subset analysis which is intended to estimate random noise in the mosaic image. To perform subset analysis, the whole data set was randomly divided into two subsets, and the difference of two subsets was taken. The difference of two subsets will erase persistent features, such as celestial sources, during observation period, and leave random noise in the mosaic image. Rms noise at the center of the noise map is about 2.7 mJy. Due to property of the scan pattern of the SCUBA-2, strength of random noise increases as goes outer parts of the mosaic image compared to the center of the mosaic image. For this study, therefore, we used the mosaic image up to the radius of 9′15 where rms noise becomes 1.5 times

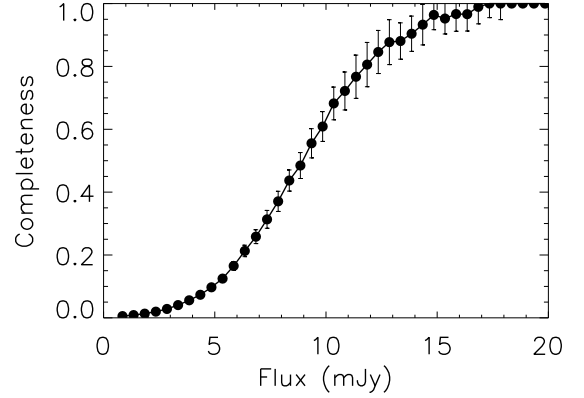


**Figure 4.** Completeness of the mosaic image. It was estimated by a recovered ratio of the injected objects. Filled circles and error bars represent median and standard deviation of 100 iterations, respectively. The 50% completeness is about 9 mJy. Relatively large error at the bright side is due to small number of artificial objects in the simulation.

of the value at the center. We selected  $S/N = 3.5$  as a threshold for the source detection because, as shown in Figure 2, the contribution of sources appears at  $S/N > 3.5$ . Although, there are some pixels above the detection threshold in the noise map, it is inevitable to ensure a number of sources for the study. We extracted 17 sources whose raw flux densities were measured from pixel value of any single isolated pixel with  $S/N > 3.5$  or peak pixel value among a group of consecutive pixels with  $S/N > 3.5$  (Figure 1).

### 3. NUMBER COUNT

#### 3.1. Simulation

In order to estimate number count of sources at 850  $\mu\text{m}$  precisely, one needs to take into account flux boosting, completeness and false detection rate in the data in advance. For this, we conducted simulation by injecting artificial objects in the noise map. Injected flux density of artificial objects ranges from 0.1 to 20.1 mJy with the step of 0.5 mJy. We determined the number of artificial objects to be added in the noise map by adopting the empirical number count estimation from Casey et al. (2013). Because observed raw flux density of a source in the observation image is affected by neighbor sources as well as random noise, the number of



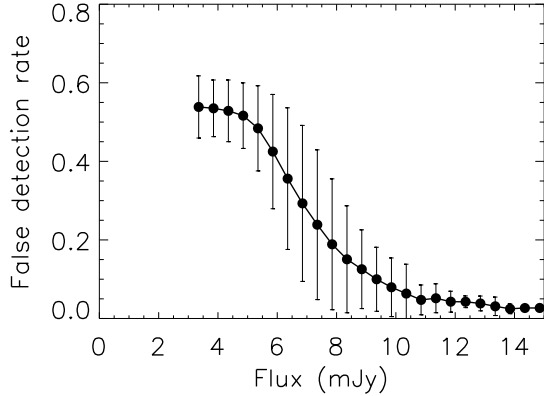


**Figure 5.** False detection rate as a function of flux density. It was estimated using the number of detected objects without any injected objects around them. Filled circles and error bars represent median and standard deviation of 100 iterations, respectively. We used different noise map for each iteration in order to obtain a result independent of the choice of the noise map. Large error represents a significant contribution of the noise map to the result of simulation. This is the reason why we adopted different noise map for each iteration.

artificial objects in the simulated map should follow the real number density of 850  $\mu\text{m}$  sources in order to estimate the contribution of neighbor sources properly. We made 10 simulated maps by adjusting the spatial distribution of artificial objects randomly on the noise map, and then conducted pre-processing (e.g., matched-filter procedure) and photometry in the same way as the observation image. This procedure was repeated 100 times by changing the noise map. Because the noise map is made by subtracting the two subsets of the data set, we can make many kinds of noise maps by randomly dividing the whole data set into two subsets. Although every noise map has almost same statistical property as a whole, e.g., same rms noise at the center and same patterns of increase towards the outer part of the noise map, it has somewhat different spatial structure in detail. Because such differences can lead to different results, we considered many noise maps to obtain generalized result of the simulation. In total, 1,000 simulated maps and about 700,000 artificial objects were used for the simulation. Flux boosting was estimated as the ratio of detected flux density to injected flux density after searching detected object within half the beam size (i.e., matching radius =  $7''$ ) around injected object (Figure 3). Completeness was estimated by counting recovered ratio of the injected objects within  $7''$  around injected object (Figure 4). False detection rate was estimated using the number of detected objects without any injected objects within  $7''$  (Figure 5). We also estimated positional uncertainty by measuring the offset between detected and injected position after searching detected object within the beam size (i.e., matching radius =  $14''$ ) around injected object (Figure 6).

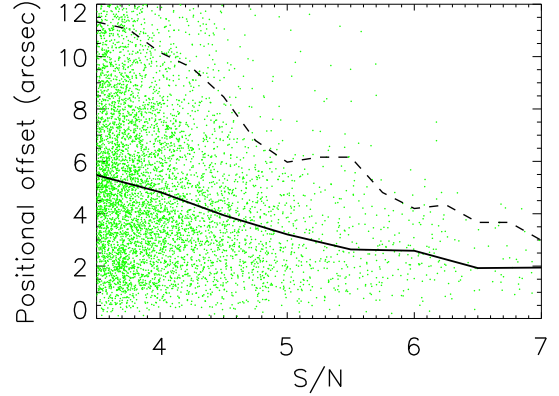


**Figure 6.** The result of simulation for positional uncertainty at 850  $\mu\text{m}$ . It was estimated by measuring the offset between detected and injected position of the artificial object. Small dot represents a result of individual artificial object. Solid line and dashed line represent median and 90% confidence interval, respectively. The sum of positional uncertainty with 90% confidence interval (dashed line) and a half of FWHM of PSF at 24  $\mu\text{m}$  was used as the matching radius when searching counterpart at 24  $\mu\text{m}$ .

### 3.2. Number Count at 850 $\mu\text{m}$

By using the results of simulation, we estimated the number count of 850  $\mu\text{m}$  sources (Figure 7). First of all, raw flux densities were deboosted using the result in Figure 3 before the estimation of number count. Raw number count in each bin,  $N$ , was determined from 17 sources with  $S/N > 3.5$ , and then properly scaled by the area and bin width. Corrections for completeness and false detection rate were obtained using results of the simulation. An error in the number count was estimated based on Poisson error ( $=\sqrt{N}$ ), and then uncertainties due to the completeness and false detection rate were added by applying the error propagation formula (Bevington & Robinson 1992, page 43). In order to confirm the validity of the error of number count based on Poisson error, we conducted simulations which estimate the error in the number count by using flux error of the source. To translate flux error of the source into the error in the number count, we made a simulated catalog without consideration of clustering by adding random error to the flux density of each source. The random error for a source is generated by a probability distribution which assumes a Gaussian function with a standard deviation of the flux error of the source. As a whole, we made 10,000 simulated catalogs and estimated number count for each simulated catalog separately. The error in the number count was determined by a standard deviation of 10,000 simulated number counts, and then errors of completeness and false detection rate were also added as before. Because this simulation considers migration of sources across bins due to addition of random errors to the flux densities of sources, it is hard to obtain reliable errors for bins in the edge especially at the faint end. For this reason, the result of this simula-

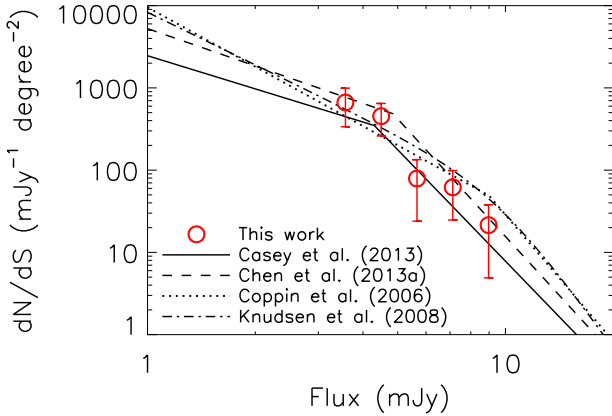


**Figure 7.** Differential number count of 850  $\mu\text{m}$  sources (open circles and error bars). The errors were estimated based on Poisson error, and then uncertainties due to the completeness and false detection rate were added using error propagation formula. Results of previous studies are presented in the functional form of double power law (dot-dashed line) or broken power law (others). Previous studies used samples taken by the SCUBA (dotted line and dot-dashed line) and the SCUBA-2 (others). As discussed earlier, the result of Casey et al. (2013, solid line) was used as the prior number of artificial objects for the simulation.

tion is presented only for three bins at the bright side (Table 3). As shown, after averaging the asymmetric components in the result of simulation, we found that ratio of two kinds of errors are 21% at most. Therefore, we conclude that the error based on Poisson error may be acceptable despite its simplicity.

#### 4. ANALYSIS OF COUNTERPARTS

##### 4.1. Likelihood Ratio analysis

In order to investigate physical properties of individual sources, we selected four 850  $\mu\text{m}$  sources with more reliable measurements ( $S/N > 4.5$ ) whose false detection rates are less than 15%. Among the four 850  $\mu\text{m}$  sources, however, three sources were used for further analysis, while 850.2 was excluded because its optical and near-infrared counterparts are severely affected by the neighbor bright star. Counterparts in multi-wavelength bands were sought using various catalogs ranging from optical to far-infrared band: Canada-France-Hawaii Telescope Legacy Survey (CFHTLS<sup>4</sup>) T0007 Wide survey ( $u^*, g, r, i$  and  $z$  bands), UKIRT Infrared Deep Sky Survey (UKIDSS; Lawrence et al. 2007) DR9 Deep Extragalactic Survey<sup>5</sup> ( $J$  and  $K$  bands), *Spitzer* Wide-area InfraRed Extragalactic survey (SWIRE<sup>6</sup>; Lonsdale et al. 2003)/IRAC DR 2.0 & 3.0 (3.6, 4.5, 5.8 and 8.0  $\mu\text{m}$ ) and *Herschel* Multi-tiered Extragalactic Survey (HerMES; Oliver et al. 2012)

<sup>4</sup><http://www.cfht.hawaii.edu/Science/CFHTLS>

<sup>5</sup><http://www.ukidss.org/surveys/surveys.html>

<sup>6</sup>SWIRE catalog is available at <http://irsa.ipac.caltech.edu/applications/Gator>

**Table 3**  
Differential number count of 850  $\mu\text{m}$  sources

Flux (mJy)	$N$	$dN/dS$ (mJy <sup>-1</sup> deg <sup>-2</sup> )	$E_{\text{poi}}^a$	$E_{\text{sim}}^b$	$r_E^c$ (%)
3.57	4	665.1	+328.3 -328.3	-	-
4.50	6	453.6	+193.1 -193.1	-	-
5.66	2	79.08	+55.11 -55.11	+76.66 -41.54	107.2
7.13	3	61.87	+37.09 -37.09	+31.01 -54.03	114.6
8.97	2	21.45	+16.55 -16.55	+13.05 -13.05	78.85

<sup>a</sup> Error based on Poisson error.

<sup>b</sup> Error based on the simulation, which was conducted in order to confirm the validity of Poisson error.

<sup>c</sup> Ratio of two kinds of errors ( $= E_{\text{sim}} / E_{\text{poi}}$ ) after averaging the asymmetric components in  $E_{\text{sim}}$ .

DR3<sup>7</sup> (24, 250, 350 and 500  $\mu\text{m}$ ). Due to large beam size of the SCUBA-2, identification of counterparts in multi-wavelength bands based on 850  $\mu\text{m}$  source is less effective. For this reason, we used the 24  $\mu\text{m}$  object in HerMES DR3 catalog as a reference object. Therefore, first of all, we searched 24  $\mu\text{m}$  objects within the matching radii of three 850  $\mu\text{m}$  sources. The matching radii were determined by the sum of positional uncertainties with 90% confidence interval of 850  $\mu\text{m}$  sources and 3'' (a half of FWHM of PSF at 24  $\mu\text{m}$ ). As shown in Figure 8, 850.3 is matched with two 24  $\mu\text{m}$  objects (850.3a for the upper 24  $\mu\text{m}$  object and 850.3b for the lower one), while others are matched with a single 24  $\mu\text{m}$  object within the matching radii. Note that, for the case of 850.4, the object denoted by dashed line box is identified at 3.6 and 4.5  $\mu\text{m}$  by eye but not detected within detection limit. Therefore, despite positional similarity with the 850  $\mu\text{m}$  source, this object was not considered in the multi-wavelength bands matching procedure. After that, we searched for optical (CFHTLS  $r$  band) counterparts within 3''/4, a half of the sum of FWHM of PSFs at two bands, around 24  $\mu\text{m}$  objects. Generally, due to higher angular resolution and detection limit of optical data than those of infrared data, it is possible that there exist multiple optical objects within the matching radius around an infrared object. In order to determine counterpart of 24  $\mu\text{m}$  object among such multiple optical candidates, we used likelihood ratio analysis (Sutherland & Saunders 1992; Smith et al. 2011; Kim et al. 2012) which considers positional offset and magnitude of an optical object at the same time.

First of all, likelihood ratio analysis was applied to the 24  $\mu\text{m}$  object and the optical (CFHTLS  $r$  band) object. We estimated a parameter  $L$  for each optical candidate within the matching radius around a certain 24  $\mu\text{m}$  object. The parameter  $L$  mainly consists of two parts: magnitude part and position part following

<sup>7</sup>A catalog for *Herschel*/SPIRE flux densities measured at *Spitzer*/MIPS 24  $\mu\text{m}$  prior positions (Lonsdale et al. 2003) by the method described in Roseboom et al. (2010). Data are available at <http://hedam.lam.fr>

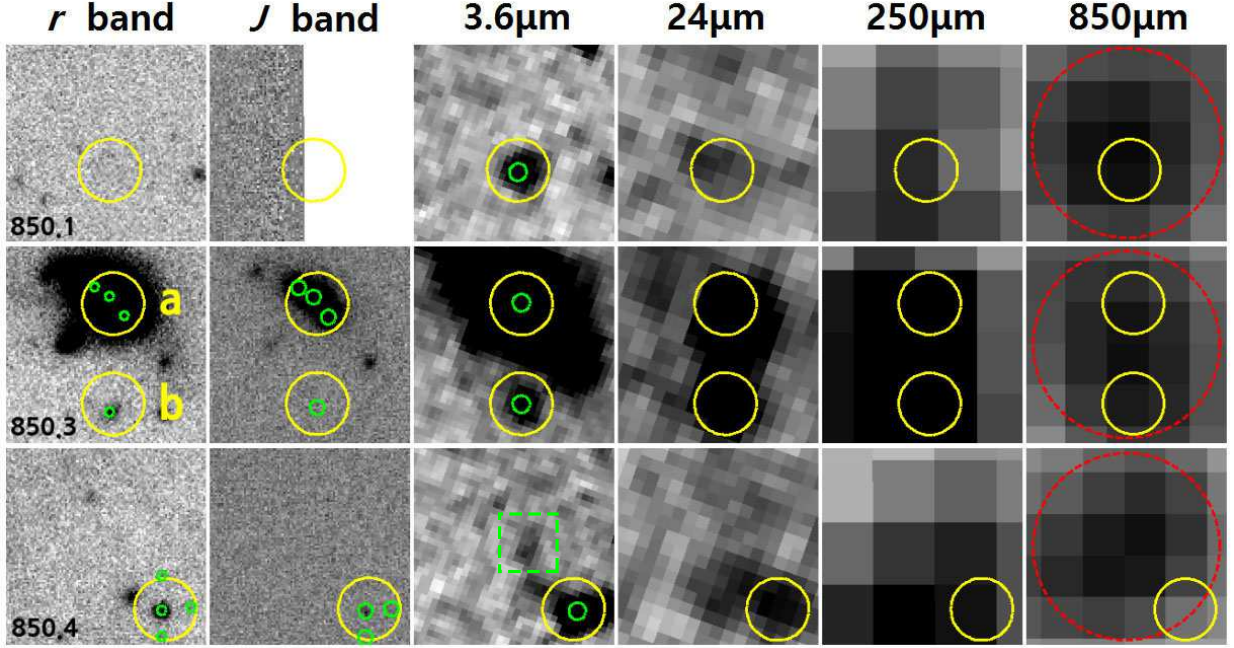


**Figure 8.** Stamp images for multi-wavelength bands. Each stamp is an inverted grey color map with the size of  $19'' \times 19''$ . From left to right, the images are CFHTLS Wide survey  $r$  band, UKIDSS  $J$  band, *Spitzer*/IRAC  $3.6 \mu\text{m}$ , *Spitzer*/MIPS  $24 \mu\text{m}$ , *Herschel*/SPIRE  $250 \mu\text{m}$  and SCUBA-2  $850 \mu\text{m}$ , respectively. Red dashed line circle represents the matching radius centered at  $850 \mu\text{m}$  source for identifying  $24 \mu\text{m}$  object, which is the sum of positional uncertainty with 90% confidence interval at  $850 \mu\text{m}$  and a half of FWHM of PSF at  $24 \mu\text{m}$ . Yellow circles correspond to the positions of  $24 \mu\text{m}$  objects with the size of FWHM of PSF. Green circles are objects in each band, which are matched with  $24 \mu\text{m}$  objects. The size of green circles represents the FWHM of PSF for each band. In the bottom row, the object denoted by dashed line box is identified at  $3.6$  and  $4.5 \mu\text{m}$  by eyes but not detected in the detection limit.

Sutherland & Saunders (1992) as expressed below.

$$L = \frac{q(m)f(r)}{n(m)} \quad (1)$$

The magnitude part consists of  $n(m)$  and  $q(m)$  which are magnitude distributions of optical objects for background and true counterpart of  $24 \mu\text{m}$  object, respectively, while position part  $f(r)$  represents probability distribution for the radial offset of the optical object from the  $24 \mu\text{m}$  object. To estimate parameters in Equation (1), we used extended HerMES DR3 and CFHTLS  $r$  band catalogs as well as 2MASS All Sky Survey (Skrutskie et al. 2006), which cover  $1^\circ \times 1^\circ$  centered at  $(\alpha_{2000}, \delta_{2000}) = (02^h18^m00^s, -04^\circ12'00'')$  and enclose the mosaic image of SCUBA-2  $850 \mu\text{m}$  in Figure 1.  $f(r)$  is expressed using a Gaussian function as presented below.

$$f(r) = \frac{1}{2\pi\sigma^2} \exp\left(\frac{-r^2}{2\sigma^2}\right) \text{ with } \sigma^2 = \sigma_{op}^2 + \sigma_{24\mu\text{m}}^2, \quad (2)$$

where  $r$  represents the distance between the optical object and the  $24 \mu\text{m}$  object, and  $\sigma$  is a quadratic sum of positional uncertainties of the optical object and the  $24 \mu\text{m}$  object.  $\sigma_{op}$  and  $\sigma_{24\mu\text{m}}$  were estimated based on the position of objects in 2MASS catalog.  $\sigma_{op}$  of  $0''.253$  (assumption with symmetric positional uncertainty) was

obtained from the CFHTLS document<sup>8</sup>. In the same way,  $\sigma_{24\mu\text{m}}$  was estimated by comparing positions of objects in HerMES DR3 and 2MASS All Sky Survey catalogs, resulting in a value of  $0''.531$ . Resulting in a value of  $0''.588$  for  $\sigma$ .  $n(m)$  is the magnitude distribution of optical objects in the background, which was scaled in value for the same area with  $q(m)$ . In order to estimate  $q(m)$ , we found magnitude distribution of optical objects within the matching radius around  $24 \mu\text{m}$  objects, and then subtracted  $n(m)$  from it. The result represents excess magnitude distribution above background magnitude distribution of optical objects, and normalization of the result becomes  $q(m)$  as presented below.

$$q(m) = \frac{\text{excess}(m)}{\Sigma_m \text{excess}(m)} \times Q_0, \quad (3)$$

where  $Q_0$  is a fraction of counterparts which are brighter than detection limit of the optical band, and is estimated as follows.

$$Q_0 = \frac{N_{\text{candidates}} - \Sigma_m n(m)}{N_{24\mu\text{m}}}, \quad (4)$$

where  $N_{\text{candidates}}$  is the number of all optical candidates within the matching radius around  $24 \mu\text{m}$  objects, and  $N_{24\mu\text{m}}$  is the number of  $24 \mu\text{m}$  objects. For the optical band, the value of  $Q_0$  turns out to be 0.664. Note

<sup>8</sup>Table 13 in <http://terapix.iap.fr/cpl/t/T0007/doc/T0007-doc.html>



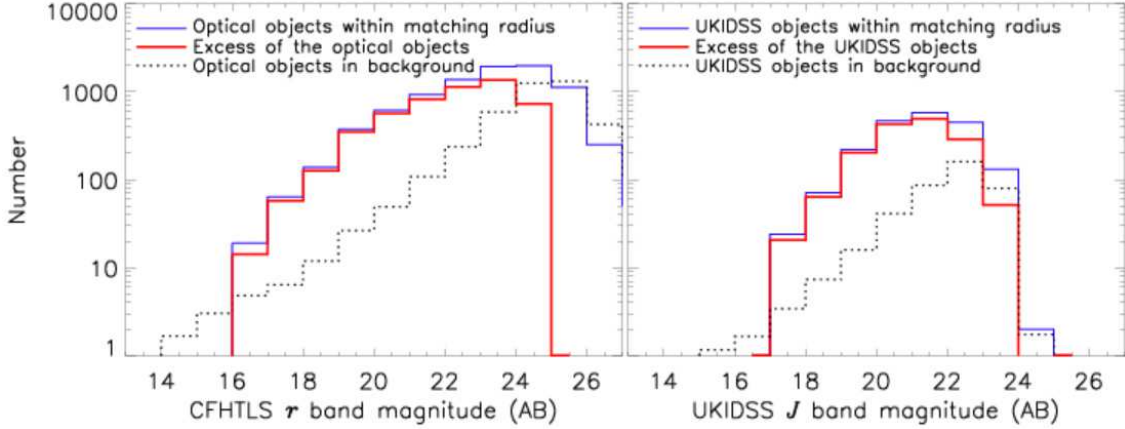


**Figure 9.** Various magnitude distributions for optical (left) and  $J$  band (right) objects. Blue thin solid line is a distribution of objects within the matching radius around  $24\ \mu\text{m}$  objects, whereas dotted line is that of objects in background after scaling in the value for the same area with the blue thin solid line. Subtraction of the two lines becomes red thick solid line which results in  $q(m)$  after the normalization in Equation (3).

that, although, as discussed in Kim et al. (2012), Equation (4) has a simple form under the assumption that there is only one optical counterpart per each  $24\ \mu\text{m}$  object, such simplicity does not change the result of likelihood ratio analysis in this study. Various magnitude distributions for optical objects are presented in the left panel of Figure 9. Reliability of the optical counterpart was estimated to confirm the validity of the identified counterpart compared with other candidates within the matching radius of a given  $24\ \mu\text{m}$  object. The reliability  $R_j$  of the optical counterpart was estimated following Sutherland & Saunders (1992):

$$R_j = \frac{L_j}{\sum_i L_i + (1 - Q_0)}, \quad (5)$$

where subscript  $i$  represents each optical candidate within the matching radius of a  $24\ \mu\text{m}$  object. In order to identify counterparts in the UKIDSS band, we performed a likelihood ratio analysis separately with parameters: positional uncertainty of  $J$  band object  $\sigma_J = 0''.266$  and  $Q_0$  for  $J$  band = 0.870. We used the extended UKIDSS catalog which covers  $0.5^\circ \times 0.5^\circ$  centered at  $(\alpha_{2000}, \delta_{2000}) = (02^h 19^m 00^s, -03^\circ 57' 11'')$ . The procedure of identifying counterparts in the  $J$  band is the same as that for optical band.

#### 4.2. SED

Likelihood ratio analysis was applied to 850.3a and 850.4 which have multiple candidates in the optical and UKIDSS bands within the matching radius around  $24\ \mu\text{m}$  object (refer to Figure 8). We estimated the value  $L$  for each candidate, and selected the one which has the largest  $L$  as the counterpart. For 850.3a, among three candidates in both optical and UKIDSS bands, the center candidate was selected as a counterpart with reliabilities of 0.910 and 0.895, respectively. For 850.4, there are four and three candidates in optical and UKIDSS bands, respectively. Among them, the center candidate (the nearest one to  $24\ \mu\text{m}$  object) was selected as

a counterpart with reliabilities of 0.994 and 0.995, respectively. Judging from the reliability values of counterpart, although we do not present a lower limit of the reliability, the result of 850.4 is highly reliable, while that of 850.3a is less reliable and there is a probability of false association. Therefore, as presented below, we choose different candidate as a counterpart of 850.3a regardless of the result of likelihood ratio analysis by using spectroscopic data and SED analysis. Although, among three candidates of 850.3a, the center object has the largest  $L$ , we choose the right one (having the second largest  $L$ ) as a real counterpart of 850.3a. According to the spectroscopic study of SDSS BOSS program (Bolton et al. 2012; Dawson et al. 2013), the center object is classified as a galaxy, while the right one is classified as a starburst galaxy by analysis of strong emission line. We also confirmed that the center object is fitted with elliptical galaxy model in wavelength range up to  $5.8\ \mu\text{m}$  band using Le Phare code<sup>9</sup> (Arnouts et al. 1999; Ilbert et al. 2006, 2009) with Polletta galaxy template (Polletta et al. 2007). For this reason, we determined the right object as a counterpart of 850.3a because it may give a larger contribution to the flux density in the  $850\ \mu\text{m}$  band than the center one. In Section 5, we estimate SFR based on  $\text{H}\alpha$  emission line flux of the counterpart of 850.3a to confirm whether it is the correct counterpart.

We adopted publicly available spectroscopic and photometric redshifts information (Table 4) for  $850\ \mu\text{m}$  sources except 850.1. Photometric redshift of 850.1 was estimated by fitting flux densities in all detected wavelength bands with the Polletta galaxy template. We used Le Phare code for SED fitting, and extinction was estimated by Calzetti law (Calzetti 2001). SED of 850.1 is best fitted by a starburst galaxy model with extinction free parameter of  $E(B - V) = 0.1$ , resulting in  $z$  and  $1\sigma$  error values of 3.284 (+0.076, -0.083). To confirm this photometric redshift esti-

<sup>9</sup><http://www.cfht.hawaii.edu/~arnouts/lephare.html>



**Table 4**  
Four 24  $\mu\text{m}$  objects that contribute to three 850  $\mu\text{m}$  sources

ID	RA <sub>24</sub> (h:m:s)	DEC <sub>24</sub> (d:m:s)	RA <sub>850</sub> (h:m:s)	DEC <sub>850</sub> (d:m:s)	Flux <sub>850</sub> <sup>a</sup> (mJy)	(S/N) <sub>850</sub>	( $\Delta P$ ) <sub>850</sub> (arcsec)	$z$
850.1	2:17:59.3	-4:06:28.2	2:17:59.4	-4:06:25.6	8.71 $\pm$ 3.77	5.3	6.2	3.284 <sup>c</sup>
850.3 <sup>b</sup>	-	-	2:18:18.9	-4:03:31.7	7.89 $\pm$ 3.43	5.1	6.0	-
850.3a	2:18:18.8	-4:03:27.7	-	-	4.25 $\pm$ 3.20	-	-	0.359 <sup>d</sup>
850.3b	2:18:18.8	-4:03:37.4	-	-	4.17 $\pm$ 3.23	-	-	3.150 <sup>e</sup>
850.4	2:18:09.8	-4:08:08.7	2:18:10.2	-4:08:02.7	7.61 $\pm$ 3.35	5.0	6.0	1.500 <sup>d</sup>

Notes, RA<sub>24</sub> and DEC<sub>24</sub> are the positions of 24  $\mu\text{m}$  counterparts. (S/N)<sub>850</sub> is a signal-to-noise ratio for 850  $\mu\text{m}$  source. ( $\Delta P$ )<sub>850</sub> represents a positional uncertainty with 90% confidence interval for 850  $\mu\text{m}$  source, which was estimated by the simulation.

<sup>a</sup> Flux densities for 850.3a and 850.3b were estimated by 24  $\mu\text{m}$  prior position source extraction, while others were estimated by blind source extraction.

<sup>b</sup> 850.3a and 850.3b are blended at 850  $\mu\text{m}$  as 850.3 in the catalog with blind source extraction but they are deblended at 850  $\mu\text{m}$  by 24  $\mu\text{m}$  prior position source extraction. Refer to Section 4.2 for the procedure of deblending.

<sup>c</sup> Photometric redshift estimated by Le Phare code in this study.

<sup>d</sup> Spectroscopic redshift in SDSS BOSS program (Bolton et al. 2012; Dawson et al. 2013).

<sup>e</sup> Photometric redshift in *Spitzer* Wide-Area Infrared Extragalactic survey (SWIRE) catalog (Rowan-Robinson et al. 2013).

**Table 5**  
Median-likelihood of Physical parameters for 850  $\mu\text{m}$  sources

ID	$\log(L_{\text{IR}}/L_{\odot})$	$\log(\text{SFR}(\text{IR})/M_{\odot}\text{yr}^{-1})$	$\log(M_{*}/M_{\odot})$	$\log(M_{\text{D}}/M_{\odot})$	$T_{\text{D}}/\text{K}$
850.1	13.27 <sup>+0.05</sup> <sub>-0.04</sub>	3.19 <sup>+0.08</sup> <sub>-0.08</sub>	11.90 <sup>+0.21</sup> <sub>-0.31</sub>	9.20 <sup>+0.13</sup> <sub>-0.11</sub>	42.85 <sup>+7.50</sup> <sub>-4.60</sub>
850.3a	11.27 <sup>+0.10</sup> <sub>-0.04</sub>	1.30 <sup>+0.09</sup> <sub>-0.02</sub>	10.18 <sup>+0.01</sup> <sub>-0.05</sub>	8.89 <sup>+0.08</sup> <sub>-0.09</sub>	29.59 <sup>+4.19</sup> <sub>-5.70</sub>
850.3b	13.42 <sup>+0.00</sup> <sub>-0.01</sub>	3.01 <sup>+0.01</sup> <sub>-0.01</sub>	11.04 <sup>+0.01</sup> <sub>-0.00</sub>	8.90 <sup>+0.13</sup> <sub>-0.19</sub>	52.75 <sup>+4.40</sup> <sub>-6.00</sub>

Note that the error corresponds to 16th - 84th percentiles of the likelihood distribution for each parameter.

mation method, we estimated photometric redshifts of 850.3a and 850.4 in the same way, resulting in  $z = 0.372$  and 1.020, respectively, and also estimated relative difference  $\Delta z = (z_{\text{spec}} - z_{\text{phot}})/z_{\text{spec}}$  with their spectroscopic redshifts. The result shows that the mean and standard deviation of  $\Delta z$  are 0.142 and 0.252, respectively.

In order to estimate physical quantities of 850  $\mu\text{m}$  sources, SED with prior redshift information were fitted using MAGPHYS<sup>10</sup> model (da Cunha et al. 2008, 2015) which is a model package developed to analyze SEDs of galaxies and to estimate physical parameters related with the stars and the interstellar dust. We used extended version of MAGPHYS for high redshift sources at  $z > 1$  (850.1 and 850.3b) as well as a standard version for a relatively nearby galaxy (850.3a). For the case of 850.3a and 850.3b, they are deblended in *Herschel*/SPIRE bands because we used HerMES DR3 (24  $\mu\text{m}$  prior position source extraction) catalog, while they are blended at 850  $\mu\text{m}$  due to blind source extraction in this study (refer to Table 4). Because the two objects share one 850  $\mu\text{m}$  source, we tried to divide their contributions to the 850  $\mu\text{m}$  flux density. For this purpose, we used 850  $\mu\text{m}$  mosaic image before the convolution procedure in SCUBA2.MATCHED.FILTER recipe because the convolution procedure would smear out the sub-structure of 850.3. We found peak pixel at 850  $\mu\text{m}$  within the size of FWHM of PSF of 24  $\mu\text{m}$  centered at 850.3a and 850.3b, respectively, and treated the peak

pixel values as raw flux densities for 850.3a and 850.3b at 850  $\mu\text{m}$ , respectively. Because their raw flux densities are affected by each other due to their close positions, we used a Gaussian function with FWHM = 14'' to estimate such contributions and subtracted the contribution from the raw flux densities. And then, flux densities were deboosted using the result in Figure 3. As a result, flux densities for 850.3a and 850.3b at 850  $\mu\text{m}$  are 4.25 $\pm$ 3.20 and 4.17 $\pm$ 3.23 mJy, respectively. For the case of 850.3a, three *Spitzer*/IRAC bands of 3.6, 4.5 and 5.8  $\mu\text{m}$  (denoted by dotted line box in Figure 10) were excluded from the fitting procedure due to blending problems with the nearby galaxy which has comparable brightness at *J* & *K* bands and is located at 2''.4 away based on CFHTLS *r* band catalog. Because MAGPHYS model does not include the contribution of QSO, we do not fit 850.4 which is classified as a QSO by the spectroscopic study of SDSS BOSS program (Bolton et al. 2012; Dawson et al. 2013). Results of model fitting are presented in Figure 10 and physical parameters extracted from the fitted model are presented in Table 5.

## 5. DISCUSSION AND SUMMARY

In this study, we presented the number count and physical properties of 850  $\mu\text{m}$  sources in the XMM-LSS field. We used the SCUBA-2 850  $\mu\text{m}$  image having a circular area with radius of 9''.15 whose rms noise at the center is 2.7 mJy. We extracted 17 sources with S/N > 3.5 to estimate number count, and used 3 reliable sources with their counterparts in multi-wavelength bands to investigate physical properties of individual sources. Results

<sup>10</sup>MAGPHYS model is publicly available on the Web at <http://www.iap.fr/magphys>

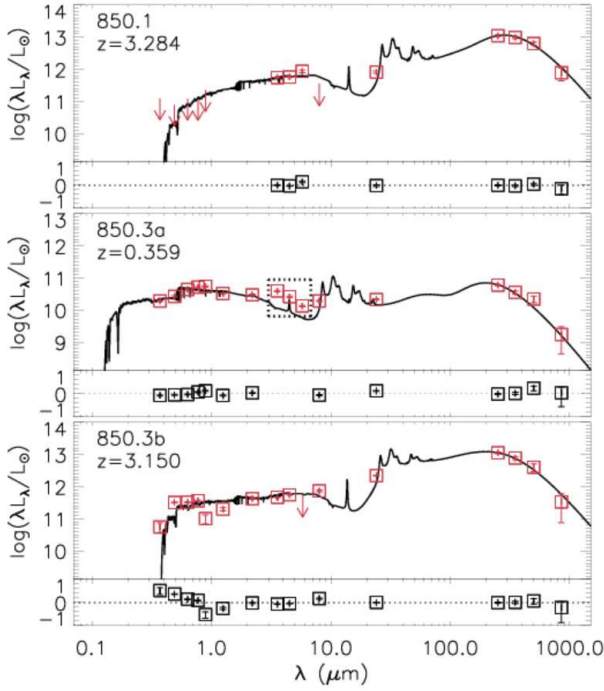


**Figure 10.** SEDs fitted by MAGPHYS model. Red squares are derived from the deboosted flux densities, black solid lines are fitted models, and the arrow indicates detection limit for each band. Black squares in the lower panel for each source represent residuals for the fitted model. For the case of 850.3a, three *Spitzer*/IRAC bands of 3.6, 4.5 and 5.8  $\mu\text{m}$  (denoted by dotted line box) were excluded from the fitting procedure due to blending problem with the neighbor galaxy.

of the study are discussed below.

1. Up to now, number count at 850  $\mu\text{m}$  has been investigated in flux range down to around 0.1 mJy. We estimated number count of 850  $\mu\text{m}$  sources in flux range between 3.5 and 9.0 mJy. Although the result of this study is not as deep as other studies, it is consistent with those of previous studies. Results in Figure 7 were derived from observation data taken by instruments with the same angular resolution (i.e., SCUBA and SCUBA-2). Coppin et al. (2006) and Casey et al. (2013) estimated number counts down to 2 mJy using sources in blank-field. The limitation of faint end flux density is related to the confusion limit. One way to overcome such limitation is using gravitational lensing effect. Knudsen et al. (2008) and Chen et al. (2013a) estimated number counts down to deeper flux ranges (0.1 and 1 mJy, respectively) using gravitationally lensed sources. Number count estimated from observation data taken by the instrument with poor angular resolution (e.g., SCUBA and SCUBA-2) is affected by a blending problem due to large beam size of the instrument. As shown in Figure 8, 850.3 consists of two objects that are likely to be resolved when observed by an instrument with higher angular resolution than the SCUBA-2. Smolčić et al. (2012) conducted observations using an interferometer with angular resolution

of  $\sim 1''$  for 28 SMGs which was previously studied using a single-dish telescope with large beam size. They found that 15–40% of SMGs are resolved into multiple objects. Hayward et al. (2013) investigated SMGs theoretically using a semi-empirical model with hydrodynamical simulations and radiative transfer, and concluded that about 30–50% of SMGs are galaxy-pairs in flux range between 3.4 and 9.2 mJy at 850  $\mu\text{m}$ . Galaxy-pairs in Hayward et al. (2013) represents infall-stage merger and, therefore, it is likely to be resolved into multiple objects when observed using high angular resolution interferometer. These studies show that number count at sub-millimeter band can be affected by angular resolution of the instrument. For this reason, the result of number count in this study should be interpreted carefully because we did not consider such issue for the estimation of number count.

2. In most studies, median redshifts of 850 & 870  $\mu\text{m}$  sources are usually known to be around  $\langle z \rangle = 2$  or larger, e.g., the median redshift is  $\langle z \rangle = 2.2$  in (850  $\mu\text{m}$ ; Chapman et al. 2005) and (870  $\mu\text{m}$ ; Wardlow et al. 2011), and redshift distribution peaks at  $\langle z \rangle = 2.16$  (850  $\mu\text{m}$ ; Casey et al. 2013). We investigated four objects which contribute to three 850  $\mu\text{m}$  sources (Table 4). Redshift distribution of them ranges from 0.36 to 3.28, which spans the results of previous studies. Clements et al. (2008) also presented similar redshift distribution  $z = 0.05$ –3.27 as ours using 33 SMGs in the SXDF survey. In this study, however, a portion of objects with  $z > 3$  is 50%, which is higher than the results of previous studies, e.g., the portion of objects with  $z > 3$  is less than 15% in the previous studies introduced above.

3. Physical parameters were extracted using MAGPHYS model, which yield infrared luminosity  $L_{\text{IR}} = 10^{11.3}$ – $10^{13.4}$   $L_{\odot}$ , SFR =  $10^{1.3}$ – $10^{3.2}$   $M_{\odot}\text{yr}^{-1}$ , stellar mass  $M_{*} = 10^{10.2}$ – $10^{11.9}$   $M_{\odot}$ , dust mass  $M_D = 10^{8.9}$ – $10^{9.2}$   $M_{\odot}$  and dust temperature  $T_D = 30$ –53 K. Such values are similar to the properties of local ULIRGs (da Cunha et al. 2010). The study for the SXDF survey also found similar infrared luminosity  $L_{\text{IR}} = 10^{10.25}$ – $10^{13.26}$   $L_{\odot}$  (Clements et al. 2008). For the case of 850.3a, H $\alpha$  emission line in SDSS BOSS program (Bolton et al. 2012; Dawson et al. 2013) gives another way for the estimation of SFR. For example, Domínguez et al. (2012) presented good agreement between SFR based on H $\alpha$  emission line and that based on far-infrared using *Herschel*/PACS sample at  $z < 0.46$ . Hwang et al. (2010a) and Lee et al. (2013) also presented good agreement between SFR(H $\alpha$ ) and SFR(IR) using local ULIRGs and star-forming galaxies at  $0.01 < z < 0.3$ , respectively. Observed H $\alpha$  and H $\beta$  emission line fluxes from the counterpart of 850.3a are 172.4 and  $33.45 \times 10^{-17}$  erg cm $^{-2}$  s $^{-1}$ , respectively. We used the factor presented in Kennicutt (1998) to convert H $\alpha$  luminosity into SFR.

$$\text{SFR(H}\alpha\text{)}[M_{\odot}\text{yr}^{-1}] = 7.9 \times 10^{-42} L_{\text{H}\alpha}[\text{erg s}^{-1}] \quad (6)$$

Rest frame bolometric luminosity  $L_{\text{H}\alpha}$  is related with

the flux as follows.

$$L_{\text{H}\alpha} [\text{erg s}^{-1}] = 4\pi d_L^2 F_{\text{H}\alpha} [\text{erg cm}^{-2} \text{s}^{-1}] \quad (7)$$

with

$$d_L = \frac{c(1+z)}{H_0} \int_0^z dz' \frac{1}{[\Omega_M(1+z')^3 + \Omega_\Lambda]^{1/2}},$$

where  $d_L$  is luminosity distance which was estimated based on the flat Universe with a set of parameters presented in Section 1. Before applying the observed  $\text{H}\alpha$  flux  $F_{\text{H}\alpha}^{\text{obs}}$  to Equation (7), it was corrected for dust extinction by following the extinction law in Calzetti et al. (2000).

$$F_{\text{H}\alpha} = F_{\text{H}\alpha}^{\text{obs}} 10^{0.4E(B-V)k(\text{H}\alpha)}, \quad (8)$$

where  $E(B-V)$  is color excess of nebular emission which was estimated using the combination of extinction law for  $\text{H}\alpha$  and  $\text{H}\beta$  as follows.

$$E(B-V) = \frac{2.5}{[k(\text{H}\beta) - k(\text{H}\alpha)]} \log \left( \frac{F_{\text{H}\alpha}^{\text{obs}}/F_{\text{H}\beta}^{\text{obs}}}{F_{\text{H}\alpha}/F_{\text{H}\beta}} \right) \quad (9)$$

with

$$\begin{aligned} k(\text{H}\alpha) &= 2.659 [-1.857 + 1.040/\lambda(\text{H}\alpha)] + R_V \\ k(\text{H}\beta) &= 2.659 [-2.156 + 1.509/\lambda(\text{H}\beta)] \\ &\quad - 0.198/\lambda^2(\text{H}\beta) + 0.011/\lambda^3(\text{H}\beta) + R_V, \end{aligned}$$

where  $\lambda(\text{H}\alpha)$  and  $\lambda(\text{H}\beta)$  are 0.65628 and 0.48613  $\mu\text{m}$ , representing rest frame wavelength for  $\text{H}\alpha$  and  $\text{H}\beta$ , respectively.  $k(\text{H}\alpha)$  and  $k(\text{H}\beta)$  are reddening curves with obscuration  $R_V = 4.05 \pm 0.80$ , which were estimated for local starburst galaxies in Calzetti et al. (2000). The flux ratio between unreddened  $\text{H}\alpha$  and  $\text{H}\beta$  is known theoretically as  $F_{\text{H}\alpha}/F_{\text{H}\beta} = 2.86$  assuming case B recombination at  $T = 10,000$  K (Osterbrock 1989), and observed flux ratio of 850.3a is  $F_{\text{H}\alpha}^{\text{obs}}/F_{\text{H}\beta}^{\text{obs}} = 5.15$ . A factor of 1.92 was multiplied in the result of Equation (8) to convert the flux contained within BOSS spectrograph with small fiber diameter ( $2''$ ) into the total flux of the galaxy. For such aperture correction, we estimated flux ratio between  $r$  band Petrosian and fiber2 (magnitude in  $2''$  aperture) magnitudes<sup>11</sup> in SDSS DR12 (Eisenstein et al. 2011; Dawson et al. 2013) following the method described in appendix A of Hopkins et al. (2003) which assumes that the radial distribution of emission line is similar with that of galaxy light. As a result, we obtained  $\log[\text{SFR}(\text{H}\alpha)/\text{M}_\odot \text{yr}^{-1}] = 1.73 (+0.16, -0.16)$ . To estimate the uncertainty of  $\text{SFR}(\text{H}\alpha)$ , we only consider the error of  $R_V$ . As shown in Table 5,  $\text{SFR}(\text{H}\alpha)$  derived from the counterpart of 850.3a is sufficient to explain  $\text{SFR}(\text{IR})$  of 850.3a, showing that the identification of the counterpart of 850.3a is correct and two other candidates of 850.3a at optical and UKIDSS bands (refer to Figure 8) hardly contribute to far-infrared and sub-millimeter bands.

<sup>11</sup>The magnitude system of SDSS is presented on the Web at <http://www.sdss.org/dr12/algorithms/magnitudes>

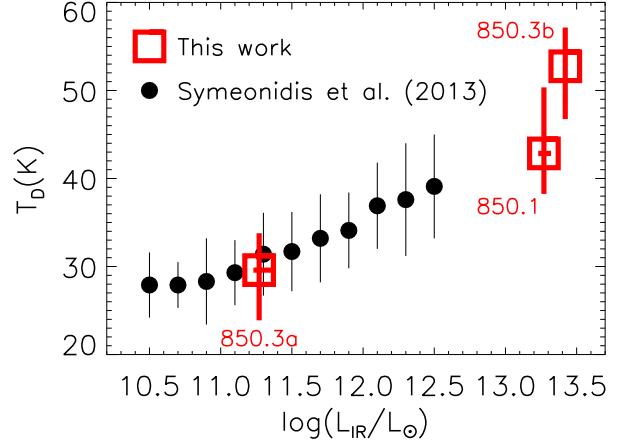


**Figure 11.**  $L_{\text{IR}}-T_D$  relation for 850  $\mu\text{m}$  sources in Table 5 (squares). IDs for 850  $\mu\text{m}$  sources are denoted by red font. Filled circles are the result of *Herschel* sample at  $0.1 < z < 2$  in Symeonidis et al. (2013), which clearly shows well-known  $L_{\text{IR}}-T_D$  relation.

4. The correlation between infrared luminosity and dust temperature ( $L_{\text{IR}}-T_D$  relation) has been known at infrared and sub-millimeter bands by observations (Chapman et al. 2005; Hwang et al. 2010b; Magnelli et al. 2012; Symeonidis et al. 2013; Smolčić et al. 2015), which show that galaxies with larger  $L_{\text{IR}}$  have warmer dust. Such relation can be explained by using Stefan-Boltzmann law (Symeonidis et al. 2013). There is also evidence that  $L_{\text{IR}}-T_D$  relation may evolve with redshift (Hwang et al. 2010b; Symeonidis et al. 2013), which show that high redshift galaxies have colder dust than local galaxies at a fixed  $L_{\text{IR}}$ . In this study, as shown in Figure 11, 850  $\mu\text{m}$  sources in Table 5 also follow the  $L_{\text{IR}}-T_D$  relation, i.e., sources with larger  $L_{\text{IR}}$  have warmer dust, and 850.3a ( $z = 0.359$ ) occupies a similar parameter space to the result of Symeonidis et al. (2013) ( $0.1 < z < 2$ ). On the other hand, the evolution of  $L_{\text{IR}}-T_D$  relation with redshift is uncertain due to the small number of samples in this study.

In order to identify the candidate protocluster around the triple SMG system as a successive study, we will obtain imaging data at 850  $\mu\text{m}$  for that area centered at the triple SMG system. The size of protocluster is usually known to be a diameter of  $\sim 2-5$  Mpc (Miley et al. 2004; Intema et al. 2006; Venemans et al. 2007). The observing mode PONG-1800 of the SCUBA-2 is suitable to cover such distance scales, observing a circular area with a diameter of  $30'$  that corresponds to 11.96 Mpc at  $z = 4.44$ . Smolčić et al. (2015) found mean infrared luminosity  $\sim 10^{13} L_\odot$  for SMGs at  $z > 4$ . If we consider this result, 850  $\mu\text{m}$  imaging data with  $3\sigma = 9.2$  mJy will be required to detect SMGs in the candidate protocluster by assuming  $L_{\text{IR}} = 10^{13} L_\odot$  starburst galaxy templates (Arp220 and M82; Polletta et al. 2007) at  $z = 4.44$ . Along with the results in this study, such imaging data will provide the criteria to identify the candidate protocluster at high redshift.



## ACKNOWLEDGMENTS

The James Clerk Maxwell Telescope is operated by the East Asian Observatory on behalf of The National Astronomical Observatory of Japan, Academia Sinica Institute of Astronomy and Astrophysics, the Korea Astronomy and Space Science Institute, the National Astronomical Observatories of China and the Chinese Academy of Sciences (Grant No. XDB09000000), with additional funding support from the Science and Technology Facilities Council of the United Kingdom and participating universities in the United Kingdom and Canada. Additional funds for the construction of SCUBA-2 were provided by the Canada Foundation for Innovation. This publication makes use of data products from the Two Micron All Sky Survey, which is a joint project of the University of Massachusetts and the Infrared Processing and Analysis Center/California Institute of Technology, funded by the National Aeronautics and Space Administration and the National Science Foundation. Based on observations obtained with MegaPrime/MegaCam, a joint project of CFHT and CEA/IRFU, at the Canada-France-Hawaii Telescope (CFHT) which is operated by the National Research Council (NRC) of Canada, the Institut National des Science de l'Univers of the Centre National de la Recherche Scientifique (CNRS) of France, and the University of Hawaii. This work is based in part on data products produced at Terapix available at the Canadian Astronomy Data Centre as part of the Canada-France-Hawaii Telescope Legacy Survey, a collaborative project of NRC and CNRS. This research has made use of data from HerMES project (<http://hermes.sussex.ac.uk/>). HerMES is a Herschel Key Programme utilising Guaranteed Time from the SPIRE instrument team, ESAC scientists and a mission scientist. The HerMES data was accessed through the Herschel Database in Marseille (HeDaM - <http://hedam.lam.fr>) operated by CeSAM and hosted by the Laboratoire d'Astrophysique de Marseille.

## REFERENCES

- Alaghband-Zadeh, S., Chapman, S. C., Swinbank, A. M., et al. 2012, Integral Field Spectroscopy of  $2.0 < z < 2.7$  Submillimetre Galaxies: Gas Morphologies and Kinematics, *MNRAS*, 424, 2232
- Aretxaga, I., Hughes, D. H., Coppin, K., et al. 2007, The SCUBA Half Degree Extragalactic Survey - IV. Radio-mm-FIR photometric Redshifts, *MNRAS*, 379, 1571
- Arnouts, S., Cristiani, S., Moscardini, L., et al. 1999, Measuring and Modelling the Redshift Evolution of Clustering: the Hubble Deep Field North, *MNRAS*, 310, 540
- Beelen, A., Omont, A., Bavouzet, N., et al. 2008, Submillimeter Observations of the J2142-4423 Ly $\alpha$  Protocluster at  $z = 2.38$ , *A&A*, 485, 645
- Bevington, P. R., & Robinson, D. K. 1992, 2nd edn., Data Reduction and Error Analysis for the Physical Sciences (New York: McGraw-Hill)
- Blain, A. W., Jameson, A., Smail, I., et al. 1999, Dust-Obscured Star Formation and AGN Fuelling in Hierarchical Models of Galaxy Evolution, *MNRAS*, 309, 715
- Bolton, A. S., Schlegel, D. J., Aubourg, É., et al. 2012, Spectral Classification and Redshift Measurement for the SDSS-III Baryon Oscillation Spectroscopic Survey, *ApJ*, 144, 144
- Calzetti, D., Armus, L., Bohlin, R. C., et al. 2000, The Dust Content and Opacity of Actively Star-forming Galaxies, *ApJ*, 533, 682
- Calzetti, D. 2001, The Dust Opacity of Star-forming Galaxies, *PASP*, 113, 1449
- Casey, C. M., Chen, C.-C., Cowie, L. L., et al. 2013, Characterization of SCUBA-2 450  $\mu$ m and 850  $\mu$ m selected galaxies in the COSMOS field, *MNRAS*, 436, 1919
- Chapin, E. L., Berry, D. S., Gibb, A. G., et al. 2013, SCUBA-2: Iterative Map-Making with the Submillimetre User Reduction Facility, *MNRAS*, 430, 2545
- Chapman, S. C., Blain, A. W., Smail, I., et al. 2005, A Redshift Survey of the Submillimeter Galaxy Population, *ApJ*, 622, 772
- Chapman, S. C., Ivison, R. J., Roseboom, I. G., et al. 2010, Herschel-SPIRE, Far-Infrared Properties of Millimetre-Bright and -Faint Radio Galaxies, *MNRAS*, 409, L13
- Chen, C.-C., Cowie, L. L., Barger, A. J., et al. 2013a, Faint Submillimeter Galaxy Counts at 450  $\mu$ m, *ApJ*, 762, 81
- Chen, C.-C., Cowie, L. L., Barger, A. J., et al. 2013b, Resolving the Cosmic Far-Infrared Background at 450 and 850  $\mu$ m with SCUBA-2, *ApJ*, 776, 131
- Clements, D. L., Vaccari, M., Babbedge, T., et al. 2008, The SCUBA Half-Degree Extragalactic Survey (SHADES) - VIII. The Nature of Faint Submillimetre Galaxies in SHADES, SWIRE and SXDF Surveys, *MNRAS*, 387, 247
- Condon, J. J., Cotton, W. D., Greisen, E. W., et al. 1998, The NRAO VLA Sky Survey, *AJ*, 115, 1693
- Coppin, K., Chapin, E. L., Mortier, A. M. J., et al. 2006, The SCUBA Half-Degree Extragalactic Survey - II. Submillimetre Maps, Catalogue and Number Counts, *MNRAS*, 372, 1621
- Coppin, K., Halpern, M., Scott, D., et al. 2008, The SCUBA Half Degree Extragalactic Survey - VI. 350- $\mu$ m Mapping of Submillimetre Galaxies, *MNRAS*, 384, 1597
- da Cunha, E., Charlot, S., & Elbaz, D. 2008, A Simple Model to Interpret the Ultraviolet, Optical and Infrared Emission from Galaxies, *MNRAS*, 388, 1595
- da Cunha, E., Charmandaris, V., Díaz-Santos, T., et al. 2010, Exploring the Physical Properties of Local Star-Forming ULIRGs from the Ultraviolet to the Infrared, *A&A*, 523, 78
- da Cunha, E., Walter, F., Smail, I. R., et al. 2015, An ALMA Survey of Sub-Millimeter Galaxies in the Extended Chandra Deep Field South: Physical Properties Derived from Ultraviolet-to-Radio Modeling, *ApJ*, 806, 110
- Dawson, K. S., Schlegel, D. J., Ahn, C. P., et al. 2013, The Baryon Oscillation Spectroscopic Survey of SDSS-III, *AJ*, 145, 10
- Dempsey, J. T., Friberg, P., Jenness, T., et al. 2013, SCUBA-2: On-Sky Calibration Using Submillimetre Standard Sources, *MNRAS*, 430, 2534
- Domínguez Sánchez, H., Mignoli, M., Pozzi, F., et al. 2012, Comparison of Star Formation Rates from H $\alpha$  and Infrared Luminosity as Seen by Herschel, *MNRAS*, 426, 330
- Edge, A., Sutherland, W., Kuijken, K., et al. 2013, The VISTA Kilo-Degree Infrared Galaxy (VIKING) Survey: Bridging the Gap between Low and High Redshift, *Msngr*, 154, 32
- Eisenstein, D. J., Weinberg, D. H., Agol, E., et al. 2011, SDSS-III: Massive Spectroscopic Surveys of the Distant

- Universe, the Milky Way, and Extra-Solar Planetary Systems, *AJ*, 142, 72
- Engel, H., Tacconi, L. J., Davies, R. I., et al. 2010, Most Submillimeter Galaxies are Major Mergers, *ApJ*, 724, 233
- Hayward, C. C., Narayanan, D., Keres, D., et al. 2013, Submillimetre Galaxies in a Hierarchical Universe: Number Counts, Redshift Distribution and Implications for the IMF, *MNRAS*, 428, 2529
- Holland, W. S., Bintley, D., Chapin, E. L., et al. 2013, SCUBA-2: the 10 000 Pixel Bolometer Camera on the James Clerk Maxwell Telescope, *MNRAS*, 430, 2513
- Hopkins, A. M., Miller, C. J., Nichol, R. C., et al. 2003, Star Formation Rate Indicators in the Sloan Digital Sky Survey, *ApJ*, 599, 971
- Hwang, H. S., Elbaz, D., Lee, J. C., et al. 2010a, Environmental Dependence of Local Luminous Infrared Galaxies, *A&A*, 522, 33
- Hwang, H. S., Elbaz, D., Magdis, G., et al. 2010b, Evolution of Dust Temperature of Galaxies through Cosmic Time as Seen by Herschel, *MNRAS*, 409, 75
- Ilbert, O., Arnouts, S., McCracken, H. J., et al. 2006, Accurate Photometric Redshifts for the CFHT Legacy Survey Calibrated Using the VIMOS VLT Deep Survey, *A&A*, 457, 841
- Ilbert, O., Capak, P., Salvato, M., et al. 2009, Cosmos Photometric Redshifts with 30-Bands for 2-deg<sup>2</sup>, *ApJ*, 690, 1236
- Intema, H. T., Venemans, B. P., Kurk, J. D., et al. 2006, Large-Scale Structure of Lyman Break Galaxies around a Radio Galaxy Protocluster at  $z \sim 4$ , *A&A*, 456, 433
- Iverson, R. J., Greve, T. R., Dunlop, J. S., et al. 2007, The SCUBA HALF Degree Extragalactic Survey - III. Identification of Radio and Mid-Infrared Counterparts to Submillimetre Galaxies, *MNRAS*, 380, 199
- Karim, A., Swinbank, A. M., Hodge, J. A., et al. 2013, An ALMA Survey of Submillimetre Galaxies in the Extended Chandra Deep Field South: High-Resolution 870  $\mu\text{m}$  Source Counts, *MNRAS*, 432, 2
- Kennicutt, R. C. Jr. 1998, Star Formation in Galaxies Along the Hubble Sequence, *ARA&A*, 36, 189
- Kim, S., Wardlow, J. L., Cooray, A., et al. 2012, *SPITZER*-IRAC Identification of *HERSCHEL*-ATLAS SPIRE Sources, *ApJ*, 756, 28
- Knudsen, K. K., van der Werf, P. P., & Kneib, J.-P. 2008, Probing the Submillimetre Number Counts at  $f_{850\mu\text{m}} < 2\text{mJy}$ , *MNRAS*, 384, 1611
- Kovács, A., Chapman, S. C., Dowell, C. D., et al. 2006, SHARC-2 350  $\mu\text{m}$  Observations of Distant Submillimetre-Selected Galaxies, *ApJ*, 650, 592
- Lagache, G., Dole, H., & Puget, J.-L. 2003, Modelling Infrared Galaxy Evolution Using a Phenomenological Approach, *MNRAS*, 338, 555
- Lawrence, A., Warren, S. J., Almaini, O., et al. 2007, The UKIRT Infrared Deep Sky Survey (UKIDSS), *MNRAS*, 379, 1599
- Lee, J. C., Hwang, H. S., & Ko, J. 2013, The Calibration of Star Formation Rate Indicators for WISE 22  $\mu\text{m}$ -Selected Galaxies in the Sloan Digital Sky Survey, *ApJ*, 774, 62
- Lonsdale, C. J., Smith, H. E., Rowan-Robinson, M., et al. 2003, SWIRE: The SIRTf Wide-Area Infrared Extragalactic Survey, *PASP*, 115, 897
- Magnelli, B., Lutz, D., Santini, P., et al. 2012, A Herschel View of the Far-Infrared Properties of Submillimetre Galaxies, *A&A*, 539, 155
- Martin, D. C., Fanson, J., Schiminovich, D., et al. 2005, The Galaxy Evolution Explorer: A Space Ultraviolet Survey Mission, *ApJ*, 619, L1
- Melnyk, O., Plionis, M., Elyiv, A., et al. 2013, Classification and Environmental Properties of X-Ray Selected Point-Like Sources in the XMM-LSS Field, *A&A*, 557, 81
- Miley, G. K., Overzier, R. A., Tsvetanov, Z. I., et al. 2004, A Large Population of ‘Lyman-Break’ Galaxies in a Protocluster at Redshift  $z \sim 4.1$ , *Nature*, 427, 4
- Mortier, A. M. J., Serjeant, S., Dunlop, J. S., A. M., et al. 2005, The SCUBA Half-Degree Extragalactic Survey - I. Survey Motivation, Design and Data Processing, *MNRAS*, 363, 563
- Oliver, S. J., Bock, J., Altieri, B., et al. 2012, The *Herschel* Multi-Tiered Extragalactic Survey: HerMES, *MNRAS*, 424, 1614
- Osterbrock, D. E. 1989, Astrophysics of Gaseous Nebulae and Active Galactic Nuclei (Mill Valley: University Science Books)
- Ouchi, M., Shimasaku, K., Okamura, S., et al. 2004, Subaru Deep Survey. VI. A Census of Lyman Break Galaxies at  $z \sim 4$  and 5 in the Subaru Deep Fields: Clustering Properties, *ApJ*, 611, 685
- Overzier, R. A., Miley, G. K., Bouwens, R. J., et al. 2006, Clustering of Star-Forming Galaxies Near a Radio Galaxy at  $z = 5.2$ , *ApJ*, 637, 58
- Polletta, M., Tajer, M., Maraschi, L., et al. 2007, Spectral Energy Distributions of Hard X-Ray Selected Active Galactic Nuclei in the XMM-Newton Medium Deep Survey, *ApJ*, 663, 81
- Roseboom, I. G., Oliver, S. J., Kunz, M., et al. 2010, The *Herschel* Multi-Tiered Extragalactic Survey: Source Extraction and Cross-Identifications in Confusion-Dominated SPIRE Images, *MNRAS*, 409, 48
- Rowan-Robinson, M., Gonzalez-Solares, E., Vaccari, M., & Marchetti, L. 2013, Revised SWIRE Photometric Redshifts, *MNRAS*, 428, 1958
- Sanders, D. B., Soifer, B. T., Elias, J. H., et al. 1988, Ultraluminous Infrared Galaxies and the Origin of Quasars, *ApJ*, 325, 74
- Skrutskie, M. F., Cutri, R. M., Stiening, R., et al. 2006, The Two Micron All Sky Survey (2MASS), *AJ*, 131, 1163
- Smail, I., Iverson, R. J., & Blain, A. W. 1997, A Deep Submillimetre Survey of Lensing Clusters: A New Window on Galaxy Formation and Evolution, *ApJ*, 490, L5
- Smith, D. J. B., Dunne, L., Maddox, S. J., et al. 2011, *Herschel*-ATLAS: Counterparts from the Ultraviolet-near-Infrared in the Science Demonstration Phase Catalogue, *MNRAS*, 416, 857
- Smolčić, V., Aravena, M., Navarrete, F., et al. 2012, Millimeter Imaging of Submillimetre Galaxies in the COSMOS Field: Redshift Distribution, *A&A*, 548, 4
- Smolčić, V., Karim, A., Miettinen, O., et al. 2015, Physical Properties of  $z > 4$  Submillimetre Galaxies in the COSMOS Field, *A&A*, 576, 127
- Sutherland, W., Emerson, J., Dalton, G., et al. 2015, The Visible and Infrared Survey Telescope for Astronomy (VISTA): Design, Technical Overview, and Performance, *A&A*, 575, 25
- Sutherland, W., & Saunders, W. 1992, On the Likelihood Ratio for Source Identification, *MNRAS*, 259, 413
- Swinbank, A. M., Lacey, C. G., Smail, I., et al. 2008, The Properties of Submm Galaxies in Hierarchical Models, *MNRAS*, 391, 420

- Symeonidis, M., Vaccari, M., Berta, S., et al. 2013, The Herschel Census of Infrared SEDs through Cosmic Time, *MNRAS*, 431, 2317
- Targett, T. A., Dunlop, J. S., Cirasuolo, M., et al. 2013, The Properties of (Sub-)Millimetre-Selected Galaxies as Revealed by CANDELS HST WFC3/IR Imaging in GOODS-South, *MNRAS*, 432, 2012
- Venemans, B. P., Kurk, J. D., Miley, G. K., et al. 2002, The Most Distant Structure of Galaxies Known: A Protocluster at  $z = 4.1$ , *ApJ*, 569, L11
- Venemans, B. P., Röttgering, H. J. A., Miley, G. K., et al. 2007, Protoclusters Associated with  $z > 2$  Radio Galaxies. I. Characteristics of High Redshift Protoclusters, *A&A*, 461, 823
- Wardlow, J. L., Smail, I., Coppin, K. E. K., et al. 2011, The LABOCA Survey of the Extended Chandra Deep Field-South: a Photometric Redshift Survey of Submillimetre Galaxies, *MNRAS*, 415, 1479
- Wright, E. L., Eisenhardt, P. R. M., Mainzer, A. K., et al. 2010, The Wide-Field Infrared Survey Explorer (WISE): Mission Description and Initial On-Orbit Performance, *AJ*, 140, 1868
- Zemcov, M., Blain, A., Halpern, M., & Levenson, L. 2010, Contribution of Lensed SCUBA Galaxies to the Cosmic Infrared Background, *ApJ*, 721, 424